Received: 1 February 2023 | Revised: 7 August 2023 | Accepted: 25 August 2023

DOI: 10.1002/mrm.29867

RESEARCH ARTICLE

Magnetic Resonance in Medicine

Incorporating the effect of white matter microstructure in the estimation of magnetic susceptibility in ex vivo mouse brain

Anders Dyhr Sandgaard[1] | **Valerij G. Kiselev**[2] | **Rafael Neto Henriques**[3] | **Noam Shemesh**[3] | **Sune Nørhøj Jespersen**[1,4]

[1]Center for Functionally Integrative Neuroscience, Department of Clinical Medicine, Aarhus University, Aarhus, Denmark

[2]Division of Medical Physics, Department of Radiology, University Medical Center Freiburg, Freiburg, Germany

[3]Champalimaud Research, Champalimaud Centre for the Unknown, Lisbon, Portugal

[4]Department of Physics and Astronomy, Aarhus University, Aarhus, Denmark

Correspondence
Sune Nørhøj Jespersen, Center for Functionally Integrative Neuroscience, Department of Clinical Medicine, Aarhus University, Aarhus, Denmark.
Email: sune@cfin.au.dk

Funding information
Danmarks Frie Forskningsfond, Grant/Award Number: 8020-00158B; Lundbeck BrainComet, Grant/Award Number: R310-2018-3455

Abstract

Purpose: To extend quantitative susceptibility mapping to account for microstructure of white matter (WM) and demonstrate its effect on ex vivo mouse brain at 16.4T.

Theory and Methods: Previous studies have shown that the MRI measured Larmor frequency also depends on local magnetic microstructure at the mesoscopic scale. Here, we include effects from WM microstructure using our previous results for the mesoscopic Larmor frequency $\overline{\Omega}^{\mathrm{Meso}}$ of cylinders with arbitrary orientations. We scrutinize the validity of our model and QSM in a digital brain phantom including $\overline{\Omega}^{\mathrm{Meso}}$ from a WM susceptibility tensor and biologically stored iron with scalar susceptibility. We also apply susceptibility tensor imaging to the phantom and investigate how the fitted tensors are biased from $\overline{\Omega}^{\mathrm{Meso}}$. Last, we demonstrate how to combine multi-gradient echo and diffusion MRI images of ex vivo mouse brains acquired at 16.4T to estimate an apparent scalar susceptibility without sample rotations.

Results: Our new model improves susceptibility estimation compared to QSM for the brain phantom. Applying susceptibility tensor imaging to the phantom with $\overline{\Omega}^{\mathrm{Meso}}$ from WM axons with scalar susceptibility produces a highly anisotropic susceptibility tensor that mimics results from previous susceptibility tensor imaging studies. For the ex vivo mouse brain we find the $\overline{\Omega}^{\mathrm{Meso}}$ due to WM microstructure to be substantial, changing susceptibility in WM up to 25% root-mean-squared-difference.

Conclusion: $\overline{\Omega}^{\mathrm{Meso}}$ impacts susceptibility estimates and biases susceptibility tensor imaging fitting substantially. Hence, it should not be neglected when imaging structurally anisotropic tissue such as brain WM.

KEYWORDS

Larmor frequency, magnetic microstructure, magnetic susceptibility, mesoscopic Lorentz sphere, modeling, quantitative susceptibility mapping

1 | INTRODUCTION

QSM[1–4] is a commonly utilized MRI methodology for mapping tissue susceptibility. Its application in disease is highly promising for imaging changes in tissue iron, calcium and myelin.[5–8] Voxel-specific tissue magnetic susceptibility can be estimated from the gradient-recalled echo (GE) signal phase. By assuming the slope of the GE phase (the Larmor frequency shift Ω) relates to the induced magnetic field of the magnetized tissue, the magnetic susceptibility can be estimated by inverting this measured magnetic field offset as a simple Fourier space product of the main-field induced magnetization with the Lorentz-corrected dipole kernel[9] Υ. This relation holds however in general only for isotropic media with scalar susceptibility.

One of the shortcomings of the current QSM framework is the neglect of mesoscopic field effects associated with microstructure and anisotropic susceptibility. This assumption is especially challenged in white matter (WM) tissue, where field perturbations from WM axons have been observed to depend on the orientation to the external field.[10–15]

A measurable orientational dependence of the magnetic field – here termed *magnetic anisotropy* – may originate from different underlying length scales. On the macroscopic scale, the overall sample shape gives rise to an orientation dependent field–including the effect of multiple tissue regions with different magnetic properties such as WM and gray matter. Such types of magnetic anisotropy are already considered in QSM or susceptibility tensor imaging[16] (STI), which extends QSM to a tensor valued susceptibility. A measured magnetic anisotropy can also stem from microscopic field effects far below the sampling resolution (sub-voxel). This naturally occurs due to microscopic susceptibility anisotropy, such as the alkyl chains in the myelin sheaths.[17–19] However, anisotropy also arises in systems with only a scalar susceptibility arranged in a microscopically anisotropic structure. We refer to these two distinct origins of magnetic anisotropy as *microscopic susceptibility anisotropy* and *microscopic structural anisotropy*, respectively, to separate from macroscopic effects. Note that macroscopic strategies, such as STI, are affected by both micro- and macroscopic magnetic anisotropy but cannot distinguish between the two, as mesoscopic field effects are unaccounted for in the STI framework. Wharton and Bowtell[20] measured the frequency shift outside a fresh porcine optic nerve, and estimated the contribution from the sample, assumed to have both isotropic and anisotropic susceptibility components, with high precision. They found that the susceptibility anisotropy contributed around five times less to the measured frequency shift than the isotropic susceptibility component. This suggests that a minimal extension to QSM that captures magnetic anisotropy should incorporate mesoscopic field effects arising from structural anisotropy but could neglect susceptibility anisotropy to a first approximation. This would also account for the effects of WM orientation dispersion, which can greatly affect mesoscopic frequencies[21] and constitute a substantial part of the total Larmor frequency[20] shift.

Recently, we outlined a framework describing the MRI measured Larmor frequency shift $\overline{\Omega}_{\mathrm{MRI}}(\mathbf{R})$.[21] We investigated microstructural effects for a population of long solid cylinders with scalar susceptibility and arbitrary orientation dispersion and found that the mesoscopic contribution depends on $l = 2$ Laplace expansion coefficients, p_{2m}, of the fiber orientation distribution function (fODF). These findings bridge the gap between fully parallel and uniformly dispersed cylinders previously used to describe microstructural field effects from cylinders,[10–13] without the need to assume a low volume fraction.[10]

Here we use this framework to address one of the shortcomings of QSM, namely, the unaccounted for mesoscopic frequency shifts, to present a minimal biophysical model of the MRI measurable Larmor frequency offset. We combine Larmor frequency measurements with fODF information (p_{2m}) obtained by fiber ball imaging[22] (FBI) diffusion MRI (dMRI). This enables estimation of the voxel-averaged (bulk) scalar magnetic susceptibility of our model that includes orientation dependent mesoscopic frequency shifts in WM but without the need for imaging at multiple sample orientations. This is different to previous studies[23,24] using information from DTI[25] to estimate the orientation of the STI susceptibility tensors, which neglected any form of structural anisotropy and mesoscopic frequency shifts. To our knowledge, only one previous study[15] has included a mesoscopic frequency shift from axially symmetric WM axons with scalar susceptibility to QSM, where the fitted susceptibility from the standard QSM-part reflected the total bulk scalar susceptibility from WM myelin, iron etc. Estimating both parameters required sample rotations and the orientation dependence was approximated by the primary eigenvector of the DTI diffusion tensor. Corrections due to the local frequency shift from chemical exchange has also been considered previously[26] in QSM.

Here we use the estimated fODF to determine a WM specific local mesoscopic contribution to the MRI Larmor frequency, representing a novel contrast based on combined information from susceptibility and fODF. We argue that this model captures the predominant effects contributing to the measured Larmor frequency shift,

equivalent to making the following three approximations (**P1**–**P3**), which we justify in the Theory section:

P1) Magnetic anisotropy of myelin is mainly caused by microscopic structural anisotropy with the magnetic susceptibility approximated as a scalar.
P2) The variance in the voxel-wise bulk susceptibilities of iron in highly structurally anisotropic WM is less than the variance in bulk susceptibility of myelin.
P3) Additional exchange-related frequency effects in myelin water are subdominant to the total measured Larmor frequency related to susceptibility.

For this, we extend our model[21] for solid cylinders to multi-layered cylinders to describe the mesoscopic frequency shifts from the WM microstructure with approximately scalar susceptibility.

Here, we investigate the parameter accuracy of QSM compared to our new framework by constructing a digital susceptibility brain phantom from dMRI images that includes both isotopic and anisotropic susceptibility of WM, and an iron-related scalar susceptibility in both WM and gray matter (GM). We find that our model improves fitting over QSM as long as the variance of myelin bulk susceptibility is greater than that of bulk WM iron susceptibility. This is also true when the absolute mean of bulk WM iron is lower than the myelin bulk susceptibility. We further simulate the frequency shift acquired at multiple sample directions, where frequency shifts from WM susceptibility anisotropy are turned on or off. By applying STI,[16,27,28] we investigate the fitted tensor susceptibility originating exclusively from unaccounted mesoscopic frequency shifts from the WM microstructure with only scalar susceptibility. This reveals a major bias in the apparent susceptibility tensor from microscopic structural anisotropy, which turns out to be much greater than the effect from actual susceptibility anisotropy (microscopic and macroscopic). Last, we apply our model framework for the frequency shift $\overline{\Omega}_{\mathrm{MRI}}(\mathbf{R})$ to experimental MGE and dMRI data obtained in ex vivo mouse brain. We estimate the voxel averaged Larmor frequency, and show that mesoscopic frequency shifts can be of the same order of magnitude to the measured frequency shift, and change susceptibility estimation in highly structural anisotropic WM.

2 | THEORY

We start by outlining the considered system, along with a brief summary of the framework for the MRI measured position-dependent Larmor frequency[21] $\overline{\Omega}_{\mathrm{MRI}}(\mathbf{R})$ based on the principle of coarse graining and by using a mesoscopic Lorentz sphere construction.[29–32] Then we extend our solution for the Larmor frequency from infinite solid cylinders with arbitrary orientation dispersion to include multilayer cylinders as shown in Figure 2.

2.1 | System of consideration

We describe the macroscopic sample of volume V as a porous medium consisting of impermeable microscopic magnetic inclusions, for example, myelin lipid bilayers. The spatial organization of the inclusions is represented by the microscopic indicator function $\nu(\boldsymbol{r})$, which is 1 inside inclusions and 0 otherwise. This defines the *microstructure* (depicted as cylinders in Figure 1D). We assume inclusions are dia- or paramagnetic, and uniformly magnetized along the applied field $\mathbf{B}_0 = B_0\widehat{\mathbf{B}}$, where $\widehat{\mathbf{B}}$ is a unit vector (as are all hatted vectors in what follows). The magnetization is described by a microscopic magnetic susceptibility $\chi(\boldsymbol{r}) \propto \nu(\boldsymbol{r})$ being on the order of ppm and given relative to the susceptibility of water (see Supporting Information S1 for a detailed description of referencing).

2.2 | Modeling a population of multilayered cylinders

The MRI measured Larmor frequency shift $\overline{\Omega}_{\mathrm{MRI}}(\mathrm{t};\mathbf{R})$ of the gradient-echo signal $S(t;\mathbf{R})$ is perturbed by local magnetic field variations induced by the tissue. Here $\mathbf{R}$ denotes the center of the voxel, t the echo time (TE), and the bar denotes averaging on the sub-voxel mesoscopic scale. As shown in previous studies,[21,30,31,33] $\overline{\Omega}_{\mathrm{MRI}}(\mathbf{R})$ can be decomposed into two contributions depending on the distance to $\mathbf{R}$ and t (in the absence of background sources).

$$\overline{\Omega}_{\mathrm{MRI}}(t;\mathbf{R}) = \overline{\Omega}^{\mathrm{Meso}}(t;\mathbf{R}) + \overline{\Omega}^{\mathrm{Macro}}(\mathbf{R}) + \overline{\Omega}_{\mathrm{Ref}}(\mathbf{R}) \qquad (1)$$

where $\overline{\Omega}^{\mathrm{Macro}}(\mathbf{R})$ captures the time independent frequency induced by distant sources on the macroscale (Figure 1C) and depends on the sample shape,

$$\overline{\Omega}^{\mathrm{Macro}}(\mathbf{R}) = \gamma B_0 \widehat{\mathbf{B}}^{\mathrm{T}} \sum_{\mathbf{R}'} \overline{\boldsymbol{\Upsilon}}(\mathbf{R}-\mathbf{R}')\overline{\chi}(\mathbf{R}')\widehat{\mathbf{B}} \qquad (2)$$

where $\overline{\boldsymbol{\Upsilon}}(\mathbf{R}-\mathbf{R}')$ is the voxel-averaged dipole kernel centered at every sampling position $\mathbf{R}'$. $\overline{\Omega}_{\mathrm{Ref}}(\mathbf{R})$ defines the frequency offset[21] at $\mathbf{R}$ from the chosen reference susceptibility and is removed upon background field removal.[34] The dipole field is denoted $\boldsymbol{\Upsilon}$ to underscore its relation to $l=2$ spherical harmonics Y_2^m and the symmetric trace-free

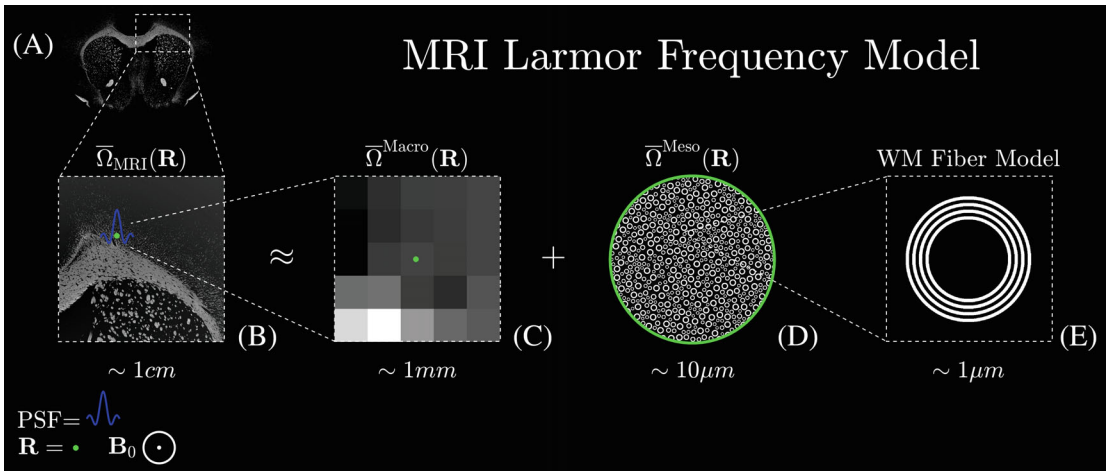

FIGURE 1 Model of the MRI Larmor frequency. (A): Myelin-stained coronal slice of mouse brain. (B): The MRI measured Larmor frequency $\overline{\Omega}_{\mathrm{MRI}}(\mathbf{R})$, coarse grained on the mesoscopic scale and sampled at discrete points $\mathbf{R}$. Sampling is described by the point-spread-function (PSF), here shown as a blue sinc-function, whose width is macroscopic. For a slowly varying magnetic microstructure, $\overline{\Omega}_{\mathrm{MRI}}(\mathbf{R})$ can be approximated by the following two contributions: (C) The macroscopic contribution approximated at the scale of the sampling resolution capturing contributions at macroscopic distances; and (D) the contribution from nearby magnetic microstructure within a mesoscopic Lorentz sphere. The latter contains here randomly placed multi-layered cylinders, one of which is depicted in (E). Mouse brain image is reproduced from © 2011 Allen Institute for Brain Science, Allen Mouse Brain Connectivity Atlas, https://connectivity.brain-map.org.

tensors (STF) $\mathscr{Y}_{2m}$ corresponding to an irreducible rank-2 representation of SO(3).[35] Supporting Information S1 (see Figure S1) explains this referencing in more detail, including a simulation demonstrating the removal of $\overline{\Omega}_{\mathrm{Ref}}(\mathbf{R})$. $\overline{\Omega}^{\mathrm{Meso}}(t;\mathbf{R})$ is a time dependent frequency offset induced by explicit magnetic microstructure in the mesoscopic vicinity of $\mathbf{R}$ (Figure 1D).[36] When $S(t;\mathbf{R})$ is measured in either the static dephasing regime or diffusion narrowing regime,[37] $\overline{\Omega}^{\mathrm{Meso}}(t;\mathbf{R}) = \overline{\Omega}^{\mathrm{Meso}}(\mathbf{R}) + \mathcal{O}(t)$ is a power law series in time, where the time independent term $\overline{\Omega}^{\mathrm{Meso}}(\mathbf{R})t$ approximates the first signal cumulant for weak dephasing. This result is also valid for non-exchanging compartments in the weak static dephasing and diffusion narrowing regime. The first cumulant is convenient as it describes the mean frequency sampled by the point-spread-function. Assuming that the magnetic microstructure varies slowly compared to the imaging resolution, with a locally uniform scalar magnetic susceptibility (as shown in Figure 1A),

$$\overline{\Omega}^{\mathrm{Meso}}(\mathbf{R}) \approx \gamma B_0 \hat{\mathbf{B}}^{\mathrm{T}} \mathbf{L}(\mathbf{R}) \hat{\mathbf{B}}, \quad \text{(Slowly varying microstructure).} \tag{3}$$

Here $\mathbf{L}(\mathbf{R})$ is the mesoscopic Lorentzian tensor.[13,21,33] For uniform susceptibility $\mathbf{L}(\mathbf{R}) = -\chi(\mathbf{R})\mathbf{N}(\mathbf{R})$ where $\mathbf{N}(\mathbf{R})$ is a mesoscopic demagnetization tensor[21] depending only on structural correlations near $\mathbf{R}$, and $\chi(\mathbf{R})$ is the local magnetic susceptibility of cylinders. We previously derived $\mathbf{N}(\mathbf{R})$ for a population of solid long cylinders exhibiting arbitrary orientation dispersion.[21] In WM fibers, water resides not only outside cylinders, but also in the intra-axonal space and myelin bilayers. In Supporting Information S2 we extend our cylinder model to include multilayer cylinders (as shown in Figure 2) and show that $\mathbf{N}(\mathbf{R})$ is in fact identical to the result for solid cylinders. This means that the mean Larmor frequency in any water compartment is indistinguishable from that in any other for this magnetic microstructure. The model-specific MRI Larmor frequency $\overline{\Omega}_{\mathrm{MRI}}(\mathbf{R})$, Eq. (1), finally becomes

$$\overline{\Omega}_{\mathrm{MRI}}(\mathbf{R}) = \gamma B_0 \Bigg(-\overline{\chi}(\mathbf{R}) \frac{1}{3} \sum_{m=-2}^{2} p_{2m}(\mathbf{R}) \mathrm{Y}_{2m}(\hat{\mathbf{B}}) \mathrm{M}^{\mathrm{WM}}(\mathbf{R}) + \hat{\mathbf{B}}^{\mathrm{T}} \sum_{\mathbf{R}'} \overline{\boldsymbol{\Upsilon}}(\mathbf{R}-\mathbf{R}') \overline{\chi}(\mathbf{R}') \hat{\mathbf{B}} \Bigg) + \overline{\Omega}_{\mathrm{Ref}}(\mathbf{R}). \tag{4}$$

The first term in Eq. (4) is $\overline{\Omega}^{\mathrm{Meso}}(\mathbf{R})$. Here $\overline{\chi}(\mathbf{R})$ defines the mesoscopically averaged (bulk) magnetic susceptibility, $\mathrm{M}^{\mathrm{WM}}(\mathbf{R})$ is a binary mask of WM (not to be mistaken for the magnetization). The orientation dependence is captured by the $l = 2$ Laplace expansion coefficients $p_{2m}(\mathbf{R})$ of the fODF measurable with dMRI,[22,38,39] and Y_{2m} is the $l = 2$ spherical harmonics. Eq. (4) differs from the conventional QSM by the presence of a mesoscopic contribution from local magnetic microstructure,[13,21,33] and by using a voxel averaged dipole field $\overline{\boldsymbol{\Upsilon}}$ as opposed to the elementary field[4] $\boldsymbol{\Upsilon}$. We have previously shown with simulations[21] that both can have a substantial effect on estimating Larmor frequencies.

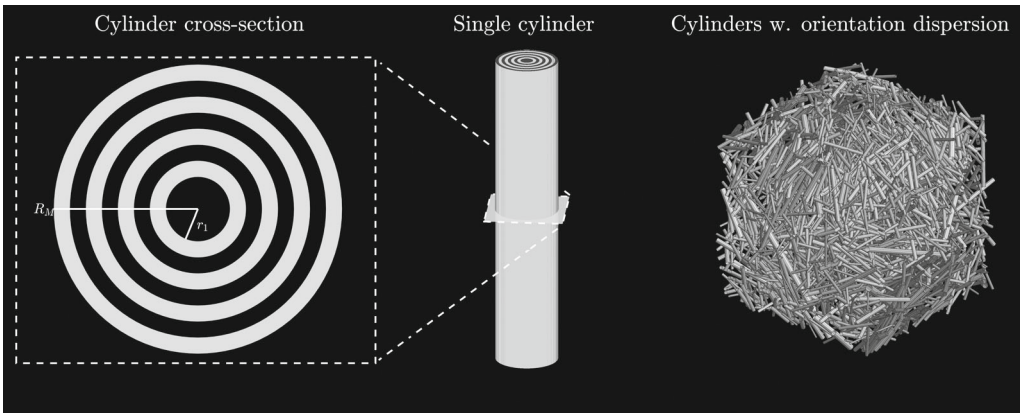

FIGURE 2 Structural model of the WM mesoscopic environment: Each fiber is modelled as M concentric cylinders of radii r_j to R_j (small/capital letters indicate inner/outer radii) with $j = 1, \ldots, M$. The cross-sectional volume fraction of the m'th fiber is $\zeta_m = \pi \sum_j \left(R_j^2 - r_j^2\right)$. The mesoscopic environment consists of N fibers with overall cross-sectional volume fraction $\zeta = \sum_m \zeta_m$ and a given orientation dispersion assumed to be independent of fiber positions and radii. Cylinders are impermeable with water uniformly distributed intra- and extra-cylindrical, and in between bilayers.

2.3 | Frequency contributions from WM susceptibility anisotropy

The microscopic susceptibility tensor $\boldsymbol{\chi}$ for a single lipid pointing along $\hat{\mathbf{u}}$ constituting the myelin sheet of a multilayer cylinder with axial direction $\hat{\mathbf{n}}$ is

$$\boldsymbol{\chi} = \left(\chi - \frac{1}{3}\Delta\chi\right)\mathbf{I} + \Delta\chi\hat{\mathbf{u}}\hat{\mathbf{u}}^{\mathrm{T}} \tag{5}$$

where $\Delta\chi$ defines the susceptibility anisotropy along $\hat{\mathbf{u}}$ and $\chi = \mathrm{Tr}[\boldsymbol{\chi}]/3$ is a third of the trace.

Averaging over lipids and cylinders (denoted by $\langle\cdot\rangle$), the bulk magnetic susceptibility $\overline{\boldsymbol{\chi}}$ of many multilayer cylinders with arbitrary orientations is

$$\overline{\boldsymbol{\chi}} = \zeta\langle\boldsymbol{\chi}\rangle = \zeta\left(\chi\mathbf{I} - \frac{\Delta\chi}{2}\left(\mathbf{T} - \frac{\mathbf{1}}{\mathbf{3}}\mathbf{I}\right)\right) = \left(\overline{\chi}\mathbf{I} - \frac{\Delta\overline{\chi}}{3}\sum_{m=-2}^{2} p_{2m}\boldsymbol{\mathcal{Y}}_{\boldsymbol{2m}}\right) \tag{6}$$

where ζ is the volume fraction of the cylinders. Here we utilized the axial symmetry of the lipids for each multilayer cylinder and $\left\langle\hat{\mathbf{u}}\hat{\mathbf{u}}^{\mathrm{T}}\right\rangle = \frac{1}{2}(\mathbf{I} - \mathbf{T})$, where $\mathbf{T} = \left\langle\hat{\mathbf{n}}\hat{\mathbf{n}}^{\mathrm{T}}\right\rangle$ is the scatter matrix.[40] Using the relation $\hat{\mathbf{n}}\hat{\mathbf{n}}^{\mathrm{T}} = 1/3\mathbf{I} + 8\pi/15\sum_{m=-2}^{2}\boldsymbol{\mathcal{Y}}_{2m}\mathrm{Y}_2^m(\hat{\mathbf{n}})$, where $\boldsymbol{\mathcal{Y}}_{2m}$ are the symmetric trace-free tensors (STF) corresponding to an irreducible rank-2 representation of SO(3),[35] and representing $\langle\cdot\rangle$ as an integral with the fODF,[21] the scatter matrix $\mathbf{T}$ could be rewritten in terms of p_{2m}, the Laplace expansion coefficients of the fODF $\mathbf{T} = 1/3\mathbf{I} + 8\pi/15\sum_{m=-2}^{2}\boldsymbol{\mathcal{Y}}_{2m}p_{2m}$, leading to the last equality in Eq. (6).

The macroscopic contribution $\overline{\Omega}_{\Delta\chi}^{\mathrm{Macro}}(\mathbf{R})$, Eq. (2), due to non-zero $\Delta\chi$ is thus

$$\overline{\Omega}_{\Delta\chi}^{\mathrm{Macro}}(\mathbf{R}) = -\frac{1}{3}\hat{\mathbf{B}}^{\mathrm{T}}\sum_{\mathbf{R}'}\overline{\mathbf{Y}}(\mathbf{R}-\mathbf{R}')\Delta\overline{\chi}(\mathbf{R}')\mathrm{M}^{\mathrm{WM}}(\mathbf{R}') \times \sum_{m=-2}^{2} p_{2m}(\mathbf{R}')\boldsymbol{\mathcal{Y}}_{\boldsymbol{2m}}\hat{\mathbf{B}} \tag{7}$$

Eq. (7) gives an explicit description of the dependence of the macroscopic frequency shift on fiber orientation through p_{2m} and susceptibility anisotropy through $\Delta\overline{\chi}$. The mesoscopic contribution $\overline{\Omega}_{\chi}^{\mathrm{Meso}}(\mathbf{R})$ from χ is found by extending our previous model[21] to multilayer cylinders, cf. Eq. (4). However, no analytical results for the mesoscopic contribution $\overline{\Omega}_{\Delta\chi}^{\mathrm{Meso}}(\mathbf{R})$ from orientationally dispersed multilayer cylinders with susceptibility anisotropy $\Delta\chi$ exist. However, as described in previous work,[21] it is given by a Lorentzian tensor $\mathbf{L}_{\Delta\chi}$ which depends on a cross-correlation tensor $\boldsymbol{\Gamma}^{\nu\Delta\chi}$ between the reporting NMR-visible fluid and the anisotropic susceptibility.

2.4 | Minimal model framework for susceptibility estimation

It is well known that WM myelin includes susceptibility anisotropy due to lipid chains,[17–19] but also contributions from other sources such as iron.[41,42] In addition, a high frequency shift in myelin water is usually ascribed to exchange.[12,13,43–45] Estimating all parameters is a daunting task, especially when mesoscopic frequency shifts must be accounted for, and would generally require active sample rotations, which might not be clinically feasible.

In the pursuit of rotation-free susceptibility estimation, we propose Eq. (4) as a minimal biophysical model

framework to account only for major susceptibility sources in each voxel. This model includes the mesoscopic frequency shifts from the WM microstructure albeit with scalar susceptibility, and thus neglects susceptibility anisotropy (**P1**) – just like QSM. Neglecting WM susceptibility anisotropy as a first approximation can be justified by a previous study[20] estimating the magnitude ratio between the isotropic and anisotropic parts of WM susceptibility to be around 5:1 with high precision. WM iron, in the region of M^{WM} where we explicitly model susceptibility sources as myelin, is assumed to be uniformly distributed (**P2**). This is justified when the mean magnitude in bulk susceptibility of WM iron is lower than the bulk susceptibility of WM myelin, or when the variance in bulk susceptibility of WM iron is subdominant compared to the variance in bulk susceptibility of WM myelin susceptibility[41] (see simulation, cf. Figure 5). As shown in Section 1 in the Supporting Information (S1), we can then neglect WM iron susceptibility in $\overline{\Omega}_{\mathrm{MRI}}(\mathbf{R})$, as it re-appears in $\overline{\Omega}_{\mathrm{Ref}}(\mathbf{R})$ and as a shift in susceptibility in GM and CSF. Then, after estimating the susceptibility and referencing it to the found CSF susceptibility, WM susceptibility represents a sum over iron and myelin bulk susceptibility referenced to CSF. The contribution from myelin water (**P3**) can be disregarded by exploiting its very fast relaxation rate,[46] that is, by estimating the Larmor frequency only at TEs much greater than its relaxation time.

Next, we investigate these assumptions and the parameter accuracy of our framework compared to QSM.

3 | METHODS

3.1 | Ex vivo brain imaging

All animal experiments were preapproved by the competent institutional and national authorities and carried out according to European Directive 2010/63.

3.1.1 | Animal preparation

Animal experiments were performed on a perfusion-fixed C57BI6 mouse brain. Briefly, a mouse was euthanized prior to the experiment with pentobarbital, transcardially perfused with phosphate-buffered saline (PBS) followed by a 4% paraformaldehyde (PFA) solution. The brain was then extracted and stored in 4% PFA for about a week in a fridge at 4°C, and 37° 1 day prior to imaging so the brain could reach thermal equilibrium with the scanner room. Before imaging, the brain was washed with PBS to minimize relaxation-effects induced by the fixative.[47] The brain was subsequently placed axially in a 10 mm NMR tube and filled with Fluorinert (Sigma Aldrich, Lisbon, Portugal).

3.1.2 | MRI experiments

Experiments were performed on a 16.4T Bruker Ascend Aeon (Bruker, Karlsruhe, Germany) interfaced with an Avance IIIHD console and a 10 mm Micro5 probe equipped with gradients capable of delivering up to 3T/m in all directions. Remmi sequences (Remmi) were used to acquire 3D gradient-recalled multi-echo images (MGE) and 3D dMRI images. For all acquisitions, repetition time was kept at 20 ms, flip angle at 20°, and bandwidth of 150 kHz. The FOV for these 3D acquisitions was $10.2 \times 17.0 \times 10.2\ \mathrm{mm}^3$, matrix size $102 \times 170 \times 102$, which resulted in an isotropic resolution of $(100\ \mu\mathrm{m})^3$. For MGE, the TEs were 1.75, 3.5, … , 17.50 ms, while dMRI was acquired at 11, 12.55, … , 19.75 ms. Two experiments with four averages were acquired for the MGE leading to an SNR in WM up to 40 and 45 in GM. dMRI was acquired with b-values ranging from 1 to $3\ \mathrm{ms}/\mu\mathrm{m}^2$, with 30 directions (**exp1**). In another experiment with identical acquisition parameters, the diffusion parameters were set to $b = 5\ \mathrm{ms}/\mu\mathrm{m}^2$ and $10\ \mathrm{ms}/\mu\mathrm{m}^2$ along 75 directions (**exp2**). One average was performed for dMRI experiments leading to an SNR in WM up to 15 and 5 in GM for $b = 5\ \mathrm{ms}/\mu\mathrm{m}^2$, and 10 in WM and 2 in GM for $b = 10\ \mathrm{ms}/\mu\mathrm{m}^2$. Diffusion times for all dMRI experiments were $\delta/\Delta = 3/6$ ms. The sample was kept at 37°C constantly during acquisition. Acquisition time was 2 h for MGE and 53 h for dMRI, where the sample should retain its tissue structure. No histology was performed after imaging.

3.1.3 | Data processing

Data processing was done in Matlab (The MathWorks, Natick, MA, USA). All complex MRI images were denoised using tensor MP-PCA[48,49] with a window size of [7 7 7], and subsequently Gibbs-unrung[50] using the complex denoised images.

3.1.4 | MGE pipeline

The complex signal phase was fitted to a linear function $\phi(t) = \left[\overline{\Omega}_{\mathrm{MRI}} + \overline{\Omega}_{\mathrm{Bgf}} + \overline{\Omega}_{\mathrm{Ref}}\right] t + \phi_0$ based on the TEs above 20 ms, where ϕ_0 accounts for unwanted B_1 effects. The frequency $\overline{\Omega}_{\mathrm{MRI}} + \overline{\Omega}_{\mathrm{Bgf}} + \overline{\Omega}_{\mathrm{Ref}}$ was then unwrapped using SEGUE,[51] and the Laplacian Boundary Value method[52] (LBV) was utilized for removing $\overline{\Omega}_{\mathrm{Bgf}} + \overline{\Omega}_{\mathrm{Ref}}$. Figure S2 in

the supporting material gives an overview of the MGE pipeline showing both raw images, and the different processing steps for the phase.

3.1.5 | dMRI pipeline

Figure S3 in the supporting material gives an overview of the dMRI pipeline. We averaged the dMRI across all TEs using singular value decomposition (SVD), to extract the diffusion-weighted signal component. After this we used the signal magnitude for fODF fitting. Due to sample drift between acquiring dMRI and MGE signals, a rigid co-registration of the dMRI signal to the MGE signal was necessary to align the fODF with the MGE signal.

3.1.6 | DKI and fODF fitting algorithms

We estimated mean diffusivity (MD) and fractional anisotropy (FA) by fitting **exp1** data to the Diffusion Kurtosis Imaging[53,54] (DKI) signal expression. The fODF Laplace coefficients p_{lm} were estimated from **exp2** data using FBI,[22] which is based on the "Standard Model" of diffusion in WM[38] (SM) and assumes the extra-axonal water signal is negligible for high gradients. We set the intra-axonal diffusivity to $2\,\mu m^2/ms$. However, the effect of using a lower diffusivity on the fODF is small.[22] We used $l_{max} = 6$ for all methods.

3.1.7 | Susceptibility fitting algorithms

Susceptibility fitting was done using an iterative linear least squares algorithm (LSMR).[55] When fitting ex vivo images, where no ground truth is available, we regularized the LSMR algorithms by selecting the number of iterations that maximized curvature of the L-curve,[56,57] which depicts the trade-off between the least squares norm and the norm of the solution. Susceptibility was referenced to the PBS fluid in the lateral and third ventricles (see Supporting Information S2 for more on referencing).

Three different frequency models were considered in this study:

- **MACRO** $\overline{\chi}_{\mathrm{QSM}}$:

$$\mathrm{argmin}_{\overline{\chi}_{\mathrm{QSM}}} \left\| \overline{\Omega}_{\mathrm{MRI}}(\mathbf{R}) - \gamma B_0 \mathrm{M}^{\mathrm{Brain}}(\mathbf{R}) \hat{\mathbf{B}}^{\mathrm{T}} \sum_{\mathbf{R}'} \Upsilon(\mathbf{R}-\mathbf{R}') \overline{\chi}_{\mathrm{QSM}}(\mathbf{R}') \hat{\mathbf{B}} \right\|_2 \tag{8}$$

where $\overline{\chi}_{\mathrm{QSM}}$ denotes the susceptibility fit without mesoscopic contribution (i.e., $\overline{\Omega}^{\mathrm{Meso}}(\mathbf{R}) = 0$) and corresponds to standard QSM. Notice that we here used the elementary dipole field[9] $\Upsilon(\mathbf{R}-\mathbf{R}')$ (no bars). $\mathrm{M}^{\mathrm{Brain}}(\mathbf{R})$ is the sample mask (not magnetization) enforcing the spatial distribution of measurements inside the brain.[58]

- **MESO + MACRO** $\overline{\chi}_{\mathrm{QSM+}}$:

$$\begin{aligned} \mathrm{argmin}_{\overline{\chi}_{\mathrm{QSM+}}} \Big\| & \overline{\Omega}_{\mathrm{MRI}}(\mathbf{R}) - \gamma B_0 \mathrm{M}^{\mathrm{Brain}}(\mathbf{R}) \\ & \times \left(-\frac{1}{3} \sum_{m=-2}^{2} p_{2m}(\mathbf{R}) \mathrm{Y}_{2m}(\hat{\mathbf{B}}) \mathrm{M}^{\mathrm{WM}}(\mathbf{R}) \overline{\chi}_{\mathrm{QSM+}}(\mathbf{R}) \right. \\ & \left. + \hat{\mathbf{B}}^{\mathrm{T}} \sum_{\mathbf{R}'} \overline{\Upsilon}(\mathbf{R}-\mathbf{R}') \overline{\chi}_{\mathrm{QSM+}}(\mathbf{R}') \hat{\mathbf{B}} \right) \Big\|_2 \end{aligned} \tag{9}$$

where $\overline{\chi}_{\mathrm{QSM+}}$ denotes susceptibility fit proposed here and includes mesoscopic contribution estimated using the p_{2m} of the fODF, as well as the voxel-averaged dipole field $\overline{\Upsilon}$. Here $\mathrm{M}^{\mathrm{WM}}(\mathbf{R})$ is a WM mask based on the FA of the scatter matrix generated from the fODF threshold at 0.45. When p_{2m} are known from independent data prior to susceptibility fitting, only a single degree of freedom remains to be determined in each voxel, namely $\overline{\chi}_{\mathrm{QSM+}}$, just as in QSM.

- **STI** $\overline{\chi}_{\mathrm{STI}}$:

$$\begin{aligned} \mathrm{argmin}_{\overline{\chi}_{\mathrm{STI}}} \Big\| & \sum_{\hat{\mathbf{B}}} \Big\{ \overline{\Omega}_{\mathrm{MRI}}(\mathbf{R};\hat{\mathbf{B}}) - \gamma B_0 \mathrm{M}^{\mathrm{Brain}}(\mathbf{R}) \hat{\mathbf{B}}^{\mathrm{T}} \\ & \times \sum_{\mathbf{R}'} \Upsilon(\mathbf{R}-\mathbf{R}') \overline{\chi}_{\mathrm{STI}}(\mathbf{R}') \hat{\mathbf{B}} \Big\} \Big\|_2 \end{aligned} \tag{10}$$

where $\overline{\chi}_{\mathrm{STI}}$ denotes susceptibility fitting using STI. As for QSM, it is a purely macroscopic model, with the only difference being that now we fit a rank-2 susceptibility tensor using multiple sample (or $\hat{\mathbf{B}}$) orientations.

3.1.8 | MRI experiment with multiple sample orientations

In Supporting Information S4 we have included an MRI experiment on an ex vivo rat brain at 9.4T. Here, MGE was acquired at five different sample orientations and dMRI at one orientation. Acquisition parameters are described in S4, with imaging and data processing similar to the mouse brain. Susceptibility fitting was done using Eqs. (8) and (9) for each sample orientation, and including all orientations at once corresponding to COSMOS[59] with and without incorporating mesoscopic frequency shifts.

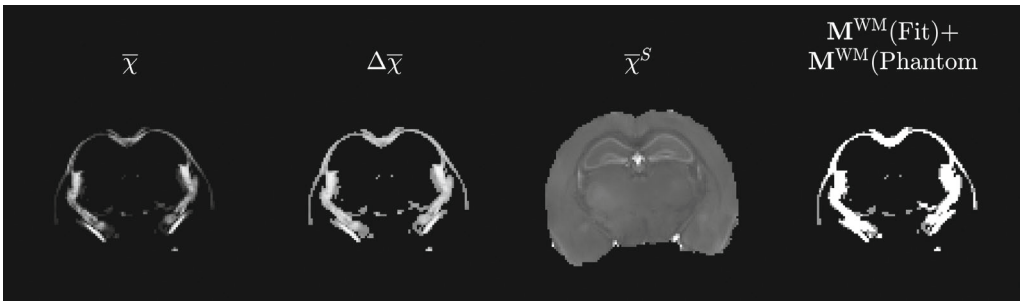

FIGURE 3 Susceptibility phantom: Synthesized magnetic susceptibility of WM and spheres (iron). WM mask M^{WM}(phantom) is generated from a high FA mask with a threshold of 0.4. For fitting we used an FA mask M^{WM} with a threshold of 0.45 to emulate an unsuccessful estimation of the total mesoscopic contribution. This is here demonstrated by their sum to show their overlap.

3.2 | Digital brain phantom simulation

We tested the accuracy in susceptibility fitting of the two models (**QSM** vs. **QSM+**) on a digital phantom (cf. Figure 3) with piece-wise constant susceptibility based on the FA and MD maps. The phantom includes both anisotropic myelin susceptibility and iron sources. We segmented the brain into WM and GM by creating a binary mask $\mathrm{M}^{\mathrm{WM}}(\mathbf{R})$ from high FA regions of the fODF scatter matrix threshold at 0.35. Notice this is lower than used in the fitting algorithm to emulate an unsuccessful segmentation of WM when fitting. From these, we synthesized four orientation invariant susceptibility parameters and computed their frequency contributions.

$$\begin{aligned}
\Delta\overline{\chi}(\mathbf{R}) &= -1 \cdot \mathrm{FA}(\mathbf{R}) \cdot \mathrm{M}^{\mathrm{WM}}(\mathbf{R}) \rightarrow \overline{\Omega}_{\Delta\chi}^{\mathrm{Meso}}(\mathbf{R}) + \overline{\Omega}_{\Delta\chi}^{\mathrm{Macro}}(\mathbf{R}) \\
\overline{\chi}(\mathbf{R}) &= 5 \cdot \mathrm{FA}(\mathbf{R}) \cdot \mathrm{M}^{\mathrm{WM}}(\mathbf{R}) \rightarrow \overline{\Omega}_{\chi}^{\mathrm{Meso}}(\mathbf{R}) + \overline{\Omega}_{\chi}^{\mathrm{Macro}}(\mathbf{R}) \\
\overline{\chi}^S_{\mathrm{WM}}(\mathbf{R}) &= \overline{\chi}^S_{\mathrm{WM}} \cdot \mathrm{MD}(\mathbf{R}) \cdot \mathrm{M}^{\mathrm{WM}}(\mathbf{R}) \rightarrow \overline{\Omega}_{\chi^S_{\mathrm{WM}}}^{\mathrm{Macro}}(\mathbf{R}) \\
\overline{\chi}^S_{\mathrm{GM}}(\mathbf{R}) &= \overline{\chi}^S_{\mathrm{GM}} \cdot \mathrm{MD}(\mathbf{R}) \cdot \left(1 - \mathrm{M}^{\mathrm{WM}}(\mathbf{R})\right) \rightarrow \overline{\Omega}_{\chi^S_{\mathrm{GM}}}^{\mathrm{Macro}}(\mathbf{R}).
\end{aligned} \tag{11}$$

The sum of all frequencies defines the ground truth $\overline{\Omega}_{\mathrm{MRI}}(\mathbf{R})$ of the phantom, assuming the reference frequency $\overline{\Omega}_{\mathrm{Ref}}(\mathbf{R})$ has been removed and no background fields were present. The ratio $\overline{\chi}/\Delta\overline{\chi}$ between the two WM susceptibilities is based on previous findings,[20] while $\overline{\chi}^S_{\mathrm{WM}}$ and $\overline{\chi}^S_{\mathrm{GM}}$ enable us to vary ratios of spherical susceptibility compared to WM. We assume mesoscopic contributions from spheres to be uniformly distributed in each voxel, so their mesoscopic contribution is zero. $\overline{\Omega}_{\chi^S_{\mathrm{GM}}}^{\mathrm{Macro}}(\mathbf{R})$ is computed like $\overline{\Omega}_{\chi}^{\mathrm{Macro}}(\mathbf{R})$ in the second term of Eq. (4).

Due to the absence of an analytical result for $\overline{\Omega}_{\Delta\chi}^{\mathrm{Meso}}$, we simulated the Lorentzian tensor $\mathbf{L}_{\Delta\chi}$ for uniformly dispersed cylinders up to a cut-off angle θ_c, as done in a similar manner in our previous study[21] (cylinder configurations can be seen in Figure S4 in Supporting Information). Randomly positioned, non-overlapping single-layered cylinders, with a ratio between inner and outer radii of 0.6, are packed with a volume fraction of 15%. Their radii are varied following a gamma distribution (see Figure S4). To compute a mesoscopic contribution $\overline{\Omega}_{\Delta\chi}^{\mathrm{Meso}}(\mathbf{R})$ in our phantom, we used the major fiber direction of the fODF along with its dispersion angle θ_{p2}[60] to define a new axially symmetric and cone shaped fODF with cut-off angle θ_{p2}. We then used our simulation as a look-up table to estimate $\overline{\Omega}_{\Delta\chi}^{\mathrm{Meso}}(\mathbf{R})$. To treat the $\overline{\Omega}_{\chi}^{\mathrm{Meso}}(\mathbf{R})$ and $\overline{\Omega}_{\Delta\chi}^{\mathrm{Meso}}(\mathbf{R})$ on equal footing, we used the same cone shaped fODF to compute their mesoscopic contributions.

Three phantoms of increasing complexity were investigated with different combinations of susceptibility. The three ground truths (GT) are shown in Figure 5 while the titles indicate the added sources. We generated the corresponding frequency shift for each phantom and added noise corresponding to an SNR = 50. We then estimated the susceptibility using either Eqs. (8) or (9). We optimized the LSMR fitting algorithm for each GT and Eqs. (8) or (9) individually, by fitting with *l2* (*Tikhonov*) regularization ranging from 1 to 0.002 in 50 logarithmically distributed steps. Through each iterative step in the LSMR algorithm, we computed the RMS error (RMSE) between our fitted susceptibility and the isotropic susceptibility sources of the GT, normalized to the norm of isotropic susceptibility sources.[61] The solution used for further analysis was then chosen based on the regularization and iteration step that minimized the RMSE. This was done to ensure a fair comparison with minimal bias caused by the ill-posed nature of the fitting problem. Upon fitting, the susceptibility maps were referenced to CSF, which we defined as having zero susceptibility.

3.2.1 | STI phantom

We also synthesized an STI phantom including only WM for simplicity. We computed the Larmor frequency (including mesoscopic frequency contributions) at 21 unique sample orientations using electrostatic repulsion,[62] both with and without susceptibility anisotropy, and then performed STI to estimate an apparent susceptibility tensor using Eq. (10). We then compared the two cases in terms of their mean magnetic susceptibility MMS = $\frac{1}{3}(\chi_1+\chi_2+\chi_3)$, susceptibility anisotropy index MSI = $|\chi_1-\chi_3|$ and color-coded MSI from the eigenvector of the eigenvalue closest to zero.[16,27]

4 | RESULTS

4.1 | Digital brain phantom

Figure 4 shows the eigenvalues for the Lorentzian tensor $\mathbf{L}_{\Delta\chi}$ from susceptibility anisotropy and isotropic susceptibility used to compute the mesoscopic frequency shift. Figure 5A shows the resulting susceptibility fits for all three phantoms with different susceptibility sources along with the difference to ground truth. It is clear from the residuals that WM is less biased for QSM+ compared to QSM. Figure 5B shows the normalized RMSE for all three phantoms for different ratios of variances $\sigma^2\left(\overline{\chi}^S_{\mathrm{WM(GM)}}(\mathbf{R})\right)/\sigma^2(\overline{\chi}(\mathbf{R}))$ between the spherical and cylindrical susceptibility in WM (variance within M^{WM}). Here we find that our constrained model has the lowest RMSE if $\sigma^2(\overline{\chi}(\mathbf{R}))$, associated with the bulk isotropic axonal susceptibility, is greater than $\sigma^2\left(\overline{\chi}^S_{\mathrm{WM}}(\mathbf{R})\right)$ of the WM iron related susceptibility. The same was true when the ratio between the mean magnitude susceptibilities $\left\langle\left|\overline{\chi}^S_{\mathrm{WM(GM)}}(\mathbf{R})\right|\right\rangle/\langle|\overline{\chi}(\mathbf{R})|\rangle$ was less than 1 (here $\langle\cdot\rangle$ denotes average across M^{WM}). Figure S5 shows the optimal number of iterations and Tikhonov regularization for QSM and QSM+. Here we find that QSM+ required more iterations but much less regularization than QSM.

4.1.1 | STI brain phantom

Figure 6 shows MMS, MSI, and color-coded MSI for the phantom with and without WM susceptibility anisotropy $\Delta\overline{\chi}$. MMS and MSI only change 10% and 12% RMSE, when adding anisotropy. This shows that the mesoscopic contribution of WM fibers with susceptibility $\overline{\chi}$ are the main source of anisotropy and not actual susceptibility anisotropy.

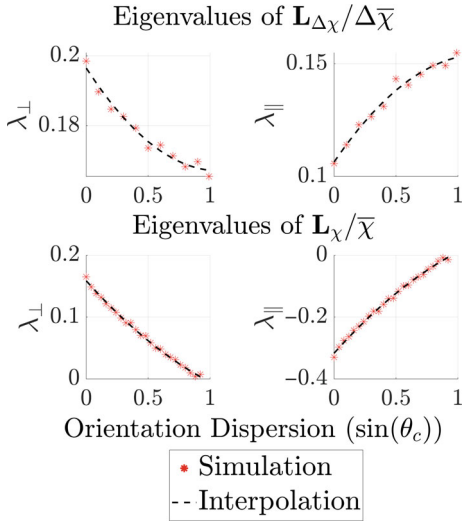

FIGURE 4 Simulation of the mesoscopic contribution from different orientation distributions: Eigenvalues $(\lambda_\perp, \lambda_\parallel)$ of the Lorentzian tensor from WM susceptibility $\mathbf{L}_{\overline{\chi}}/\overline{\chi}$ and susceptibility anisotropy $\mathbf{L}_{\Delta\overline{\chi}}/\Delta\overline{\chi}$ are presented for various levels of dispersion set by the maximum allowed polar angle θ_c. $\mathbf{L}_{\Delta\overline{\chi}}/\Delta\overline{\chi}$ was simulated for 12 different dispersions, while $\mathbf{L}_{\overline{\chi}}/\overline{\chi}$ is reproduced from previous study.[21] The black line shows the interpolation of the data to a second order polynomial, which was used as a look-up table for computing the mesoscopic frequency shifts from different fiber directions. The depicted perpendicular eigenvalue is the mean of the two perpendicular eigenvalues.

4.2 | Ex vivo brain imaging

4.2.1 | Magnetic susceptibility $\overline{\chi}$

Figure 7 shows the susceptibility maps from two different coronal slices of the mouse brain (Sagittal and horizontal slices can be seen in Figures S6 and S7, respectively). The last two rows show the susceptibility difference $\delta\overline{\chi}$ of $\overline{\chi}_{\mathrm{QSM}}$ compared to $\overline{\chi}_{\mathrm{QSM+}}$ with the fODF estimated from FBI at different b-values. We observed increased hyperintensity in highly anisotropic WM parallel to the main field such as the anterior commissure. Here we found a mean bulk WM susceptibility and SD to be around -98 ± 10 ppb (compared to -75 ± 8 when mesoscopic contributions from WM are not included), which is closer to previous findings[14,20] than QSM.

4.2.2 | Larmor frequency contributions

The macroscopic and mesoscopic contributions to the Larmor frequency were calculated using the forward relation in Eq. (3) with the estimated susceptibility and p_{2m} of the fODF as input. The result is shown in Figure 8. Figure 8A,

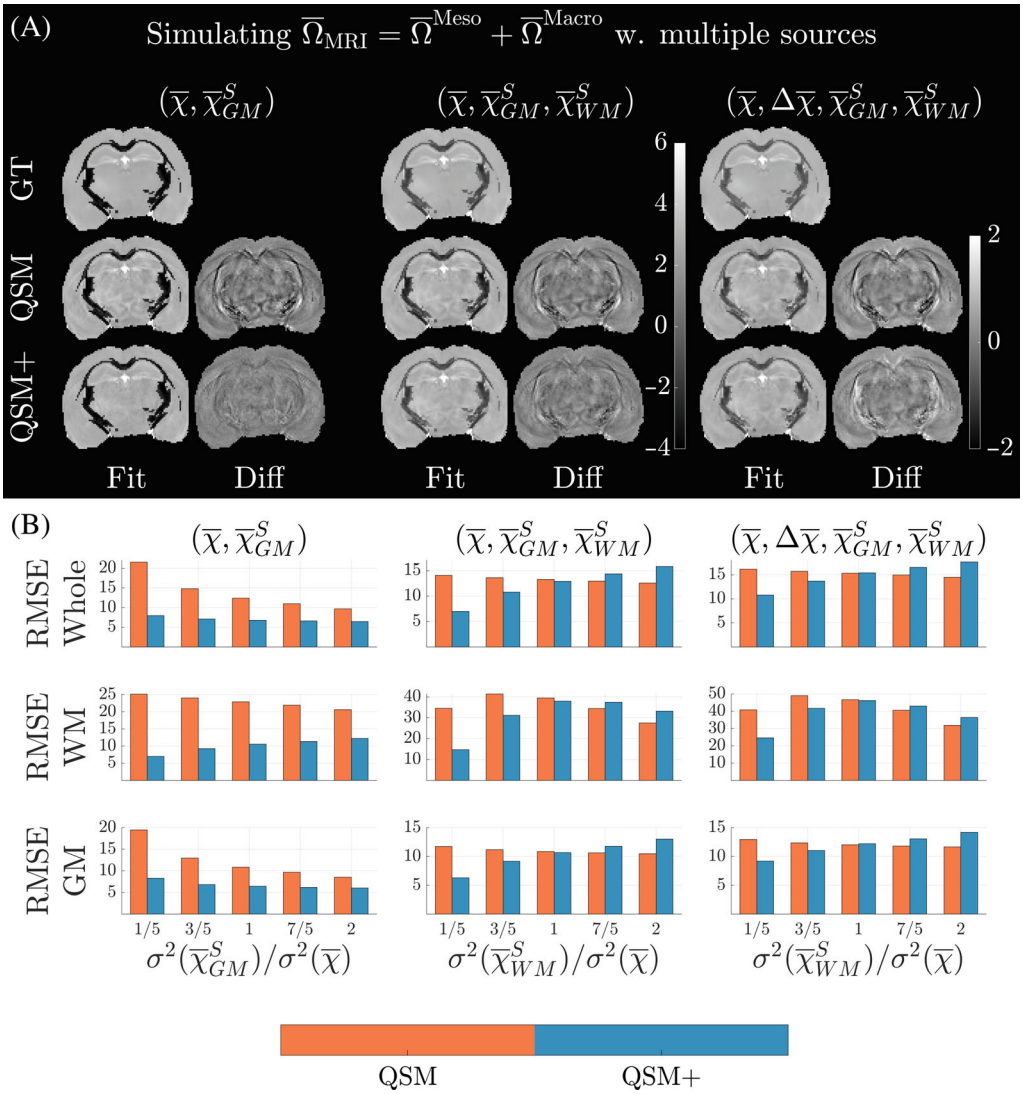

FIGURE 5 Fitting with and without adding mesoscopic frequency shifts: Three different phantoms considered with different susceptibility contributions (as shown in titles). $\overline{\chi}$ is the white matter (WM) axon susceptibility, while $\overline{\chi}^S_{\mathrm{WM}}$ and $\overline{\chi}^S_{\mathrm{GM}}$ is the spherical susceptibility in WM and gray matter (GM), respectively. (A) The first row shows the ground truth susceptibility for each of the three phantoms. Middle row shows fitting without adding mesoscopic contributions (QSM), while the bottom row shows fitting with (QSM+). Differences from ground truth are shown in the adjoining columns. SNR here is 50 with a 3/5 ratio between $\sigma^2(\overline{\chi})$ and $\sigma^2\left(\overline{\chi}^S_{\mathrm{WM}}\right)$. (B) shows bar plot of normalized (compared to isotropic susceptibility of ground truth) RMSE referenced to CSF. The x-axis shows various ratios in variance where 1/5–3/5 are WM plausible, while the remaining are GM/thalamus plausible. When $\sigma^2(\overline{\chi})$ is greater or comparable with $\sigma^2\left(\overline{\chi}^S_{\mathrm{WM}}\right)$, the lowest RMSE is achieved including mesoscopic frequency shifts to the model, even though it neglects the spatial heterogeneity of $\overline{\chi}^S_{\mathrm{WM}}$ and WM susceptibility anisotropy.

clearly show that the mesoscopic contribution is non-zero in white-matter regions, and when the field is parallel to the axon, it is positive and opposite in sign to the macroscopic contribution, as expected from theory. Figure 8B shows a 3D maximum intensity projection of $\overline{\Omega}_{\mathrm{MRI}}$, $\overline{\Omega}^{\mathrm{Meso}}$ and $\overline{\Omega}^{\mathrm{Macro}}$ (at $b = 10\,\mathrm{ms/\mu m^2}$). This demonstrates that $\overline{\Omega}^{\mathrm{Meso}}$ provides a novel contrast by combining information of both p_{2m} and $\overline{\chi}$.

4.2.3 | MRI experiment with multiple sample orientations

In Supporting Information S4, we show that the susceptibility obtained from COSMOS (cf. Figures S8 and S9) including mesoscopic frequency shifts produces slightly lower residuals with visually less structural bias in comparison to conventional COSMOS. We also find that WM susceptibility becomes more negative by the mesoscopic

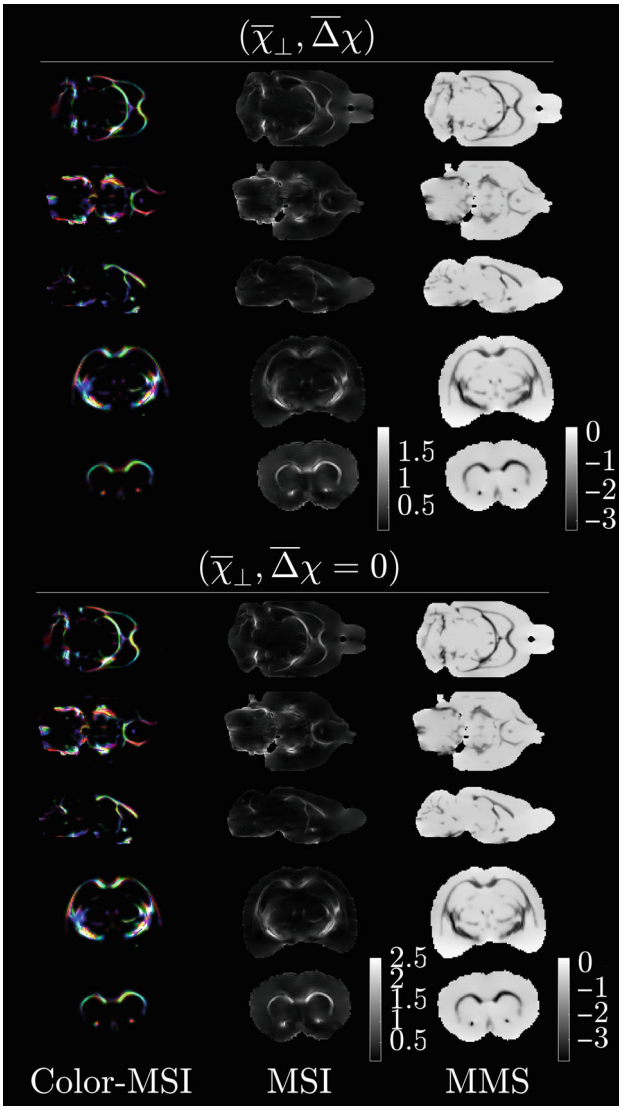

FIGURE 6 Tensor eigenvalues of susceptibility tensor imaging (STI) phantom: Fitting results from applying STI to the measured Larmor frequency (Eq. 10) of a digital phantom sampled at 21 orientations, including both mesoscopic and macroscopic frequency shifts. The upper panel shows fitting the phantom with susceptibility anisotropy, while the bottom panel has no susceptibility anisotropy. Both phantoms include structural anisotropy due to the mesoscopic contribution. Comparing the mean magnetic susceptibility (MMS), anisotropy (MSI), and color-coded MSI using the eigenvector of the most positive susceptibility eigenvalue, we find that the source of anisotropy and tractography contrast stems not from susceptibility anisotropy, but rather a bias from pure structural anisotropy from the mesoscopic contribution with scalar susceptibility $\overline{\chi}$.

correction, in agreement with the effect observed on the single orientation fit of the mouse brain (cf. Figure 7). For the single orientation susceptibility fits, we observed only a small improvement in the residuals (cf. Figure S10).

5 | DISCUSSION

5.1 | Incorporation mesoscopic field effects into QSM

Estimating magnetic susceptibility is challenging for many reasons. In particular, the MRI measured Larmor frequency shift $\overline{\Omega}_{\mathrm{MRI}}$ depends on the local organization of magnetized tissue at the mesoscopic scale. This contribution has so far not been included in standard quantitative susceptibility (QSM) models, but can potentially be responsible for a frequency shift on the same order of magnitude as the contribution from neighboring voxels, the only contribution considered in QSM.[21] In fact, this is why the average field outside long parallel randomly positioned cylinders in a cylindrical container is zero as the mesoscopic frequency shifts are equal to and opposite the macroscopic frequency contributions.

5.1.1 | Minimal magnetic microstructure model

The purpose of this study was to develop a minimal model framework for the measured Larmor frequency when sampling at multiple orientations is not feasible. Our model includes frequency shifts from the WM microstructure with microscopic isotropic susceptibility and structurally isotropic sources with isotropic susceptibility in gray matter. In reality, WM voxel contains multiple sources, for example highly aligned myelinated axons and non-heme iron.[63] However, our model offers an improvement in susceptibility estimation compared to QSM as long the variance or the mean magnitude in bulk susceptibility of, for example, WM iron is lower than for the isotropic bulk susceptibility of myelin–no matter if susceptibility anisotropy is present or not (see simulation in Figure 5).

5.1.2 | Future extensions of the biophysical model

A reasonable next step will be to analytically include mesoscopic frequency contributions from microscopic WM susceptibility anisotropy to extend our model framework. Estimating model parameters for such a model requires sampling at multiple orientations. While our model includes myelin water (MW), evidence[43,44,64] suggests a large frequency shift in MW that goes beyond our proposed susceptibility model. For that reason, we assumed MW to be fully relaxed. This is a reasonable assumption since we only considered the signal phase at

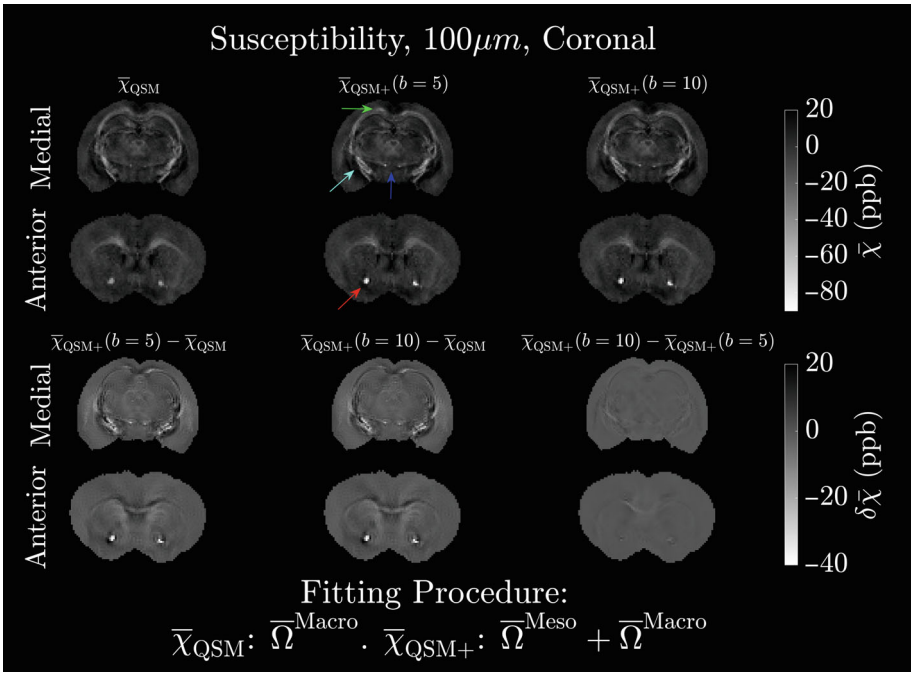

FIGURE 7 Susceptibility maps of mouse brain at 100 µm isotropic resolution: Coronal slices from the medial and anterior parts of the brain are shown. $\overline{\chi}_{QSM}$ corresponds to zero mesoscopic contribution (analogous to quantitative susceptibility mapping [QSM]), and $\overline{\chi}_{QSM+}$ corresponds to a non-zero mesoscopic contribution calculated using this method. Largest differences are visible near the cingulum and corpus callosum (green), cerebral peduncle (light blue), and anterior commissure olfactory limb (red) and mammalithalamic tract (dark blue).

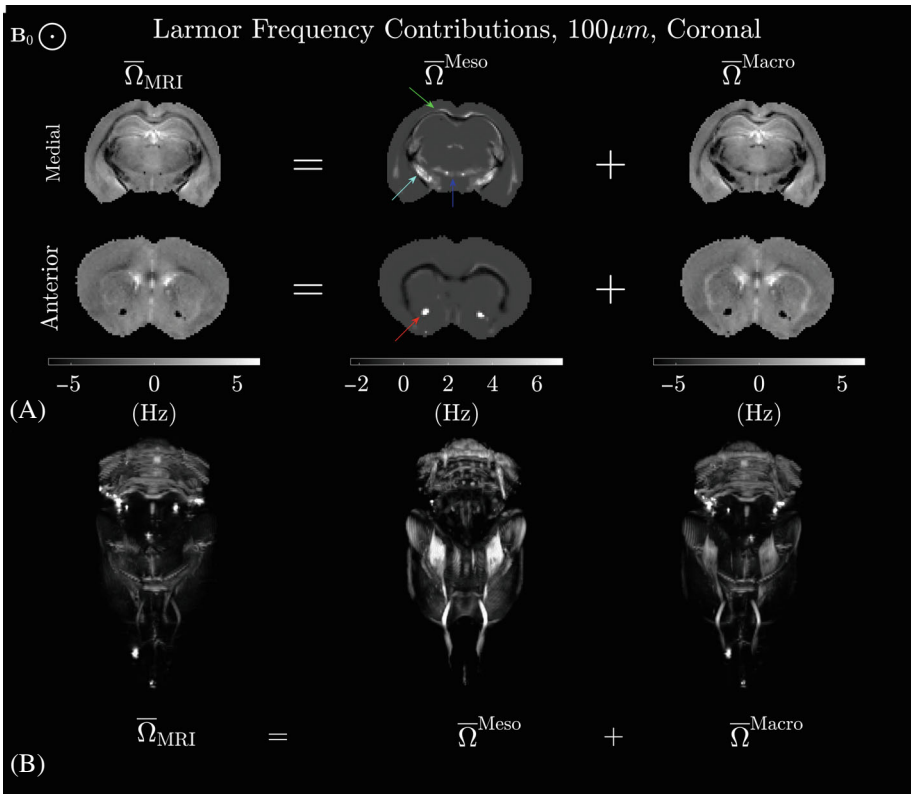

FIGURE 8 Macroscopic and mesoscopic Larmor frequencies (using $\overline{\chi}_{QSM+}$ at $b = 10\,ms/\mu m^2$): (A) The frequencies are calculated using the forward relation in Eq. (3). The biggest mesoscopic contributions to the Larmor frequency are found in regions of highly anisotropic white matter. This is especially visible near the cingulum and corpus callosum (green), cerebral peduncle (light blue), and anterior commissure olfactory limb (red) and mammalithalamic tract (dark blue). (B) Horizontal 3D rendition of mesoscopic frequency $\overline{\Omega}^{Meso}$ at $b = 10\,ms/\mu m^2$ based on the maximum intensity projection.

TEs above 20 ms, where MW should be absent at 16.4T due to its fast relaxation rate. Different mechanisms have been proposed to explain this observation,[45,65,66] and we aim to investigate it in the future in order to include MW in our model. Additional frequency shifts from various randomly oriented magnetic inclusions with scalar susceptibilities, for example, to model the effect of iron, will also be considered in the future. Modelling the signal relaxation within the same biophysical picture can also add additional information, which could be used to include for example, an iron-related susceptibility without sample rotations.[67]

5.2 | Limitations

5.2.1 | Susceptibility and frequency contributions

We estimated the bulk scalar magnetic susceptibility of an ex vivo mouse with and without including mesoscopic frequency contributions from WM (Figure 7). The susceptibility maps revealed noticeable differences in contrast and large quantitative differences. In the anterior commissure, the RMS difference in $\overline{\chi}$ was 25%, when mesoscopic contributions from WM are not considered. A similar susceptibility difference was observed in an ex vivo rat brain (Figures S8–S10 Supporting Information S4) where we included multiple sample orientations in the susceptibility fit. This underscores the impact of including microstructural field effects when quantifying magnetic susceptibility, even without including tensor $\boldsymbol{\chi}$. However, it is important to understand these mechanisms better in the future, before attempting to achieve robust susceptibility estimations and resolve multiple types of inclusions in a single voxel.

While our model only includes a single degree of freedom, we found that the ill-posed nature associated with the dipole field eroded the effect of the mesoscopic frequency shift. This was evident when comparing single orientation fits with a multi orientation fit (See Figures S8–S10 in Supporting Information S4). Here we found that the iterative LSMR algorithm used required many iterations (on the order of 100 iterations without any regularization due to having multiple orientations) in order for the residuals to be lower when incorporating the mesoscopic correction in WM. For the single orientation fits on the rat brain, we observed that the noise corrupted the fit after around 5–10 iterations, when no regularization was included. When including an $l2$ Tikhonov regularization, a higher number of iterations could be reached, but at the expense of a larger bias in susceptibility values and in the residuals in Larmor frequency–especially in WM where the susceptibility was highest, ultimately eroding the improvement by the mesoscopic correction. Hence, while our model only includes one degree of freedom, it still benefits from acquiring images at multiple sample orientations to make the inverse problem better posed, or by using better fitting algorithms with more sophisticated regularization schemes than Tikhonov regularization.

Nevertheless, while our WM model is simple compared to actual magnetic tissue microstructure, we believe the model's apparent susceptibility gives an important first insight into the relationship between mesoscopic and macroscopic frequency contributions in real data.

5.2.2 | fODF

The fODF was estimated by doing spherical decomposition of the dMRI signal at high b using FBI.[22] As a flavor of the Standard Model of diffusion in white matter[38] (SM), it models WM axons similarly to our proposed WM axon model. In comparison to DTI-derived metrics, such as FA and the primary diffusion eigenvector which describe the diffusive dispersion from both intra- and extra-axonal diffusion anisotropy, SM-derived methods estimating the fODF allows estimating the actual fiber orientation dispersion.

SM considers dispersion between bundles of parallel axons, while our susceptibility model considers dispersion between individual fibers. Nevertheless, our model is consistent with the axon configuration in SM, since bundles of randomly positioned parallel cylinders does not give rise to any additional frequency shift.[21]

Even though misestimation of the fODF will bias susceptibility estimates, only the $l = 2$ expansion coefficients, p_{2m}, of the fODF are necessary to estimate the mesoscopic frequency shifts. These are typically rather robust against noise, and with less variation across different diffusion times.[68]

It took around 53 h to acquire dMRI signals used for fODF estimation. While this is far beyond a reasonable timeframe in a clinical setting, a normal FBI protocol could be done in around 10 min on a clinical scanner.[69] Hence, QSM+ could be performed in around 12 min at 2 mm isotropic resolution in vivo. The large scan time here was chosen to achieve ultra-high isotropic resolution (100 μm isotropic) with high SNR, to reduce image artifacts and achieve optimal co-registration between dMRI and MGE voxels. For this we used a 3D acquisition with no partial Fourier acceleration or acceleration scheme such as EPI.

5.2.3 | Fixation effects

As imaging was performed on ex vivo mouse brains, effects related to fixation may also affect the estimated parameters due to structural alterations, increased chemical shifts and changes in chemical composition.[14,19,47,70] Susceptibility values have earlier been found to be numerically smaller in vivo compared to ex vivo.[14,71] For example, PBS and PFA solution can lead to increased macro-molecular exchange, earlier found to lead to shifts on the order of −0.013 ppm and 0.05 ppm, respectively.[14] Secondly, PFA susceptibility differs by −0.028 ppm compared to CSF.[14]

5.3 | Implications for QSM and STI

So far, QSM has been regarded as the best option for susceptibility estimation, when rotating the sample is not possible. Our simulations indicate that the best strategy for the simplest possible susceptibility model is to include only the largest contributor to the Larmor frequency in each voxel. In WM, this is believed to be the isotropic component of the myelin susceptibility tensor.[20,41] Eq. 3 represents the Larmor frequency shift in our model framework including mesoscopic frequency shifts from WM microstructure. As it is seen from our ex vivo fitting, including mesoscopic frequency shifts in WM can substantially change susceptibility estimation. This requires estimating the fODF at high b-value, optimally around $b = 10\,\mathrm{ms/\mu m^2}$.

STI represents a natural extension of QSM to include macroscopic tensor anisotropy while still neglecting mesoscopic frequency shifts. Numerous studies have applied the STI model as a demonstration of WM susceptibility anisotropy.[16,27,28] However, microstructurally related frequency shifts in WM produce a large bias in STI.[20] This was corroborated in a recent work[28] incorporating orientation dependent WM frequency offsets in STI fitting, resulting in a large decrease in susceptibility anisotropy on human brain. However, the susceptibility and fODF dependence in these local frequency offsets, which was demonstrated here (Figure 4) and in previous work,[21] was not included.

Our simulations reveal that a predominant source of anisotropy in the STI tensor arises instead from the mesoscopic frequency from WM microstructure with only scalar susceptibility, that is, microstructural anisotropy. In fact, the apparent anisotropy was the same order of magnitude as the mean susceptibility, and in line with experimental findings for STI.[16,27,28] We also compared our maps to known STI tractography studies,[16,27,28] and found results strikingly similar to previous studies, including their characteristic deviation from standard DTI tractography. Second, when we include actual susceptibility anisotropy, we found that this only changed the measured STI tensor around 10% root-mean-squared-difference, indicating that a large sources of anisotropy in STI may originate from a mesoscopic contribution of WM *microstructure*, and not magnetic susceptibility anisotropy.

6 | CONCLUSIONS

We developed a novel minimal framework for including mesoscopic Larmor frequency contributions in QSM, especially relevant when imaging at multiple orientations is not an option. This was done by modeling the frequency induced from WM magnetic microstructure as organized in long multi-layered cylinders with orientation dispersion and scalar susceptibility. Through computer simulations, we find that our model improves susceptibility estimation compared to QSM, and STI are substantially biased by the unaccounted-for structural anisotropy due to the mesoscopic frequency contribution, indicating the observed STI tensor might not represent susceptibility anisotropy as expected. Our experimental results show that local WM microstructure induces a substantial frequency shift in WM and should not be ignored in QSM. Susceptibility estimation based on our minimal framework could be performed in around 12 min at 2 mm isotropic resolution in vivo. We believe our results will advance the pursuit of a full characterization of magnetic microstructure of nervous tissue, with the goal of faithful parameter estimations that can be used actively in clinical research.

ACKNOWLEDGMENTS

This study is funded by the Independent Research Fund (grant 8020-00158B) and Lundbeck BrainComet R310-2018-3455. We also thank Shemesh lab members, especially Cristina Chavarrías, PhD, and Beatriz Cardoso, MSc, for assisting with MRI experiments, and Prof. Mark D Does and Dr. Kevin Harkins from Vanderbilt University for the REMMI pulse sequence.

ORCID

Noam Shemesh https://orcid.org/0000-0001-6681-5876
Sune Nørhøj Jespersen https://orcid.org/0000-0003-3146-4329

REFERENCES

1. Salomir R, de Senneville BD, Moonen CT. A fast calculation method for magnetic field inhomogeneity due to an arbitrary distribution of bulk susceptibility. *Concepts Magn Reson*. 2003;19B:26-34. doi:10.1002/cmr.b.10083
2. Marques JP, Bowtell R. Application of a Fourier-based method for rapid calculation of field inhomogeneity due to spatial variation of magnetic susceptibility. *Concepts Magn Reson Part B Magn Reson Eng*. 2005;25B:65-78. doi:10.1002/cmr.b.20034
3. Jenkinson M, Wilson JL, Jezzard P. Perturbation method for magnetic field calculations of nonconductive objects. *Magn Reson Med*. 2004;52:471-477. doi:10.1002/mrm.20194
4. Deistung A, Schweser F, Reichenbach JR. Overview of quantitative susceptibility mapping. *NMR Biomed*. 2017;30:e3569. doi:10.1002/nbm.3569
5. Eskreis-Winkler S, Deh K, Gupta A, et al. Multiple sclerosis lesion geometry in quantitative susceptibility mapping (QSM) and phase imaging. *J Magn Reson Imaging*. 2015;42:224-229. doi:10.1002/jmri.24745
6. Eskreis-Winkler S, Zhang Y, Zhang J, et al. The clinical utility of QSM: disease diagnosis, medical management, and surgical planning. *NMR Biomed*. 2017;30:e3668. doi:10.1002/nbm.3668
7. Wang Y, Spincemaille P, Liu Z, et al. Clinical quantitative susceptibility mapping (QSM): biometal imaging and its emerging roles in patient care. *J Magn Reson Imaging*. 2017;46:951-971. doi:10.1002/jmri.25693

8. Wang C, Martins-Bach AB, Alfaro-Almagro F, et al. Phenotypic and genetic associations of quantitative magnetic susceptibility in UK biobank brain imaging. *Nat Neurosci*. 2022;25:818-831. doi:10.1038/s41593-022-01074-w
9. Ruh A, Kiselev VG. Calculation of Larmor precession frequency in magnetically heterogeneous media. *Concepts Magn Reson Part A*. 2018;47A:e21472. doi:10.1002/cmr.a.21472
10. Yablonskiy DA, Haacke EM. Theory of NMR signal behavior in magnetically inhomogeneous tissues: the static dephasing regime. *Magn Reson Med*. 1994;32:749-763. doi:10.1002/mrm.1910320610
11. Kiselev VG, Posse S. Analytical model of susceptibility-induced MR signal dephasing: effect of diffusion in a microvascular network. *Magn Reson Med*. 1999;41:499-509. doi:10.1002/(SICI)1522-2594(199903)41:3
12. Wharton S, Bowtell R. Fiber orientation-dependent white matter contrast in gradient echo MRI. *Proc Natl Acad Sci U S A*. 2012;109:18559-18564. doi:10.1073/pnas.1211075109
13. Yablonskiy DA, Sukstanskii AL. Generalized lorentzian tensor approach (GLTA) as a biophysical background for quantitative susceptibility mapping. *Magn Reson Med*. 2015;73:757-764. doi:10.1002/mrm.25538
14. Luo J, He X, Yablonskiy DA. Magnetic susceptibility induced white matter MR signal frequency shifts—experimental comparison between Lorentzian sphere and generalized Lorentzian approaches. *Magn Reson Med*. 2014;71:1251-1263. doi:10.1002/MRM.24762
15. Khabipova D, Gil R, Zwiers M, Marques JP. Quantitative susceptibility mapping including a white matter Lorenzian correction. *Proc Intl Soc Mag Reson Med*. 2016;24:2861.
16. Liu C. Susceptibility tensor imaging. *Magn Reson Med*. 2010;63:1471-1477. doi:10.1002/mrm.22482
17. Lounila J, Ala-Korpela M, Jokisaari J, Savolainen MJ, Kesäniemi YA. Effects of orientational order and particle size on the NMR line positions of lipoproteins. *Phys Rev Lett*. 1994;72:4049-4052. doi:10.1103/PhysRevLett.72.4049
18. Lee J, Shmueli K, Kang BT, et al. The contribution of myelin to magnetic susceptibility-weighted contrasts in high-field MRI of the brain. *Neuroimage*. 2012;59:3967-3975. doi:10.1016/J.NEUROIMAGE.2011.10.076
19. Liu C, Li W, Johnson GA, Wu B. High-field (9.4 T) MRI of brain dysmyelination by quantitative mapping of magnetic susceptibility. *Neuroimage*. 2011;56:930-938. doi:10.1016/J.NEUROIMAGE.2011.02.024
20. Wharton S, Bowtell R. Effects of white matter microstructure on phase and susceptibility maps. *Magn Reson Med*. 2015;73:1258-1269. doi:10.1002/mrm.25189
21. Sandgaard AD, Shemesh N, Kiselev VG, Jespersen SN. Larmor frequency shift from magnetized cylinders with arbitrary orientation distribution. *NMR Biomed*. 2023;36:e4859. doi:10.1002/nbm.4859
22. Jensen JH, Russell Glenn G, Helpern JA. Fiber ball imaging. *Neuroimage*. 2016;124:824-833. doi:10.1016/j.neuroimage.2015.09.049
23. Wisnieff C, Liu T, Spincemaille P, Wang S, Zhou D, Wang Y. Magnetic susceptibility anisotropy: cylindrical symmetry from macroscopically ordered anisotropic molecules and accuracy of MRI measurements using few orientations. *Neuroimage*. 2013;70:363-376. doi:10.1016/J.NEUROIMAGE.2012.12.050
24. Li X, Vikram DS, Lim IAL, Jones CK, Farrell JAD, van Zijl PCM. Mapping magnetic susceptibility anisotropies of white matter in vivo in the human brain at 7 T. *Neuroimage*. 2012;62:314-330. doi:10.1016/J.NEUROIMAGE.2012.04.042
25. Basser PJ, Mattiello J, Lebihan D. Estimation of the effective self-diffusion tensor from the NMR spin Echo. *J Magn Reson Ser B*. 1994;103:247-254. doi:10.1006/jmrb.1994.1037
26. Schweser F, Zivadinov R. Quantitative susceptibility mapping (QSM) with an extended physical model for MRI frequency contrast in the brain: a proof-of-concept of quantitative susceptibility and residual (QUASAR) mapping. *NMR Biomed*. 2018;31:e3999. doi:10.1002/NBM.3999
27. Liu C, Li W, Wu B, Jiang Y, Johnson GA. 3D fiber tractography with susceptibility tensor imaging. *Neuroimage*. 2012;59:1290-1298. doi:10.1016/J.NEUROIMAGE.2011.07.096
28. Feng R, Cao S, Zhuang J, et al. An improved asymmetric susceptibility tensor imaging model with frequency offset correction. *Magn Reson Med*. 2022;27:828-844. doi:10.1002/MRM.29494
29. Ye FQ, Allen PS. Relaxation enhancement of the transverse magnetization of water protons in paramagnetic suspensions of red blood cells. *Magn Reson Med*. 1995;34:713-720. doi:10.1002/MRM.1910340510
30. Durrant CJ, Hertzberg MP, Kuchel PW. Magnetic susceptibility: further insights into macroscopic and microscopic fields and the sphere of Lorentz. *Concepts Magn Reson Part A*. 2003;18A:72-95. doi:10.1002/CMR.A.10067
31. He X, Yablonskiy DA. Biophysical mechanisms of phase contrast in gradient echo MRI. *Proc Natl Acad Sci U S A*. 2009;106:13558-13563. doi:10.1073/pnas.0904899106
32. Ruh A, Scherer H, Kiselev VG. The larmor frequency shift in magnetically heterogeneous media depends on their mesoscopic structure. *Magn Reson Med*. 2018;79:1101-1110. doi:10.1002/mrm.26753
33. Kiselev VG. Larmor frequency in heterogeneous media. *J Magn Reson*. 2019;299:168-175. doi:10.1016/j.jmr.2018.12.008
34. Schweser F, Robinson SD, de Rochefort L, Li W, Bredies K. An illustrated comparison of processing methods for phase MRI and QSM: removal of background field contributions from sources outside the region of interest. *NMR Biomed*. 2017;30:e3604. doi:10.1002/NBM.3604
35. Thorne KS. Multipole expansions of gravitational radiation. *Rev Mod Phys*. 1980;52:299-339. doi:10.1103/RevModPhys.52.299
36. Ruh A, Kiselev VG. Larmor frequency dependence on structural anisotropy of magnetically heterogeneous media. *J Magn Reson*. 2019;307:106584. doi:10.1016/j.jmr.2019.106584
37. Kiselev VG, Novikov DS. Transverse NMR relaxation in biological tissues. *Neuroimage*. 2018;182:149-168. doi:10.1016/j.neuroimage.2018.06.002
38. Novikov DS, Fieremans E, Jespersen SN, Kiselev VG. Quantifying brain microstructure with diffusion MRI: theory and parameter estimation. *NMR Biomed*. 2019;32:e3998. doi:10.1002/NBM.3998
39. Jeurissen B, Tournier JD, Dhollander T, Connelly A, Sijbers J. Multi-tissue constrained spherical deconvolution for improved analysis of multi-shell diffusion MRI data. *Neuroimage*. 2014;103:411-426. doi:10.1016/j.neuroimage.2014.07.061
40. Fisher NI, Lewis T, Embleton BJJ. *Statistical Analysis of Spherical Data*. Cambridge University Press; 1987. doi:10.1017/CBO9780511623059

41. Fukunaga M, Li TQ, Van Gelderen P, et al. Layer-specific variation of iron content in cerebral cortex as a source of MRI contrast. *Proc Natl Acad Sci U S A*. 2010;107:3834-3839. doi:10.1073/pnas.0911177107
42. Kirilina E, Helbling S, Morawski M, et al. Superficial white matter imaging: contrast mechanisms and whole-brain in vivo mapping. *Sci Adv*. 2020;6:eaaz9281. doi:10.1126/SCIADV.AAZ9281
43. Van Gelderen P, De Zwart JA, Lee J, Sati P, Reich DS, Duyn JH. Nonexponential T2* decay in white matter. *Magn Reson Med*. 2012;67:110-117. doi:10.1002/mrm.22990
44. Sati P, van Gelderen P, Silva AC, et al. Micro-compartment specific T2∗ relaxation in the brain. *Neuroimage*. 2013;77:268-278. doi:10.1016/J.NEUROIMAGE.2013.03.005
45. Duyn JH. Frequency shifts in the myelin water compartment. *Magn Reson Med*. 2014;71:1953-1955. doi:10.1002/mrm.24983
46. Nunes D, Cruz TL, Jespersen SN, Shemesh N. Mapping axonal density and average diameter using non-monotonic time-dependent gradient-echo MRI. *J Magn Reson*. 2017;277:117-130. doi:10.1016/J.JMR.2017.02.017
47. Birkl C, Langkammer C, Golob-Schwarzl N, et al. Effects of formalin fixation and temperature on MR relaxation times in the human brain. *NMR Biomed*. 2016;29:458-465. doi:10.1002/nbm.3477
48. Veraart J, Novikov DS, Christiaens D, Ades-aron B, Sijbers J, Fieremans E. Denoising of diffusion MRI using random matrix theory. *Neuroimage*. 2016;142:394-406. doi:10.1016/j.neuroimage.2016.08.016
49. Olesen JL, Ianus A, Østergaard L, Shemesh N, Jespersen SN. Tensor denoising of high-dimensional MRI data. *Magn Reson Med*. 2023;89:1160-1172. doi:10.1002/MRM.29478
50. Kellner E, Dhital B, Kiselev VG, Reisert M. Gibbs-ringing artifact removal based on local subvoxel-shifts. *Magn Reson Med*. 2016;76:1574-1581. doi:10.1002/mrm.26054
51. Karsa A, Shmueli K. SEGUE: a speedy region-growing algorithm for unwrapping estimated phase. *IEEE Trans Med Imaging*. 2019;38:1347-1357. doi:10.1109/TMI.2018.2884093
52. Zhou D, Liu T, Spincemaille P, Wang Y. Background field removal by solving the Laplacian boundary value problem. *NMR Biomed*. 2014;27:312-319.
53. Veraart J, Sijbers J, Sunaert S, Leemans A, Jeurissen B. Weighted linear least squares estimation of diffusion MRI parameters: strengths, limitations, and pitfalls. *Neuroimage*. 2013;81:335-346. doi:10.1016/J.NEUROIMAGE.2013.05.028
54. Jensen JH, Helpern JA, Ramani A, Lu H, Kaczynski K. Diffusional kurtosis imaging: the quantification of non-gaussian water diffusion by means of magnetic resonance imaging. *Magn Reson Med*. 2005;53:1432-1440. doi:10.1002/mrm.20508
55. Fong DCL, Saunders M. LSMR: an iterative algorithm for sparse least-squares problems. *SIAM J Sci Comput*. 2011;33:2950-2971. doi:10.1137/10079687X
56. Hansen PC, Hansen PC. The L-curve and its use in the numerical treatment of inverse problems. *Adv Comput Bioeng*. 2000;4:119-142.
57. Hansen PC, O'Leary DP. The use of the L-curve in the regularization of discrete ill-posed problems. *SIAM J Sci Comput*. 2006;14:1487-1503. doi:10.1137/0914086
58. Sandgaard AD, Shemesh N, Jespersen SN, Kiselev VG. To mask or not to mask? Investigating the impact of accounting for spatial frequency distributions and susceptibility sources on QSM quality. *Magn Reson Med*. 2023;90:353-362. doi:10.1002/MRM.29627
59. Liu T, Spincemaille P, De Rochefort L, Kressler B, Wang Y. Calculation of susceptibility through multiple orientation sampling (COSMOS): a method for conditioning the inverse problem from measured magnetic field map to susceptibility source image in MRI. *Magn Reson Med*. 2009;61:196-204. doi:10.1002/mrm.21828
60. Novikov DS, Veraart J, Jelescu IO, Fieremans E. Rotationally-invariant mapping of scalar and orientational metrics of neuronal microstructure with diffusion MRI. *Neuroimage*. 2018;174:518-538. doi:10.1016/J.NEUROIMAGE.2018.03.006
61. Marques JP, Meineke J, Milovic C, et al. QSM reconstruction challenge 2.0: a realistic in silico head phantom for MRI data simulation and evaluation of susceptibility mapping procedures. *Magn Reson Med*. 2021;86:526-542. doi:10.1002/MRM.28716
62. Jones DK, Horsfield MA, Simmons A. Optimal strategies for measuring diffusion in anisotropic systems by magnetic resonance imaging. *Magn Reson Med*. 1999;42:515-525. doi:10.1002/(SICI)1522-2594(199909)42:3<515::AID-MRM14>3.0.CO;2-Q
63. Duyn JH, Van Gelderen P, Li TQ, De Zwart JA, Koretsky AP, Fukunaga M. High-field MRI of brain cortical substructure based on signal phase. *Proc Natl Acad Sci U S A*. 2007;104:11796-11801. doi:10.1073/PNAS.0610821104
64. Nam Y, Lee J, Hwang D, Kim DH. Improved estimation of myelin water fraction using complex model fitting. *Neuroimage*. 2015;116:214-221. doi:10.1016/J.NEUROIMAGE.2015.03.081
65. Hédouin R, Metere R, Chan KS, et al. Decoding the microstructural properties of white matter using realistic models. *Neuroimage*. 2021;237:118138. doi:10.1016/j.neuroimage.2021.118138
66. Yablonskiy DA, Sukstanskii AL. Biophysical mechanisms of myelin-induced water frequency shifts. *Magn Reson Med*. 2014;71:1956-1958. doi:10.1002/mrm.25214
67. Shin H-G, Lee J, Yun YH, et al. χ-separation: magnetic susceptibility source separation toward iron and myelin mapping in the brain. *Neuroimage*. 2021;240:118371. doi:10.1016/J.NEUROIMAGE.2021.118371
68. Lee H-HH, Yaros K, Veraart J, et al. Along-axon diameter variation and axonal orientation dispersion revealed with 3D electron microscopy: implications for quantifying brain white matter microstructure with histology and diffusion MRI. *Brain Struct Funct*. 2019;224:1469-1488. doi:10.1007/s00429-019-01844-6
69. Moss HG, McKinnon ET, Glenn GR, Helpern JA, Jensen JH. Optimization of data acquisition and analysis for fiber ball imaging. *Neuroimage*. 2019;200:690-703. doi:10.1016/J.NEUROIMAGE.2019.07.005
70. Chan KS, Hédouin R, Mollink J, Schulz J, van Cappellen van Walsum AM, Marques JP. Imaging white matter microstructure with gradient-echo phase imaging: is ex vivo imaging with formalin-fixed tissue a good approximation of the in vivo brain? *Magn Reson Med*. 2022;88:380-390. doi:10.1002/MRM.29213
71. O'Callaghan J, Holmes H, Powell N, et al. Tissue magnetic susceptibility mapping as a marker of tau pathology in Alzheimer's disease. *Neuroimage*. 2017;159:334-345. doi:10.1016/j.neuroimage.2017.08.003

SUPPORTING INFORMATION

Additional supporting information may be found in the online version of the article at the publisher's website.

FIGURE S1. Susceptibility phantom WM iron and myelin including external fields: (A) shows the ground truth susceptibility $\delta\overline{\chi}_{GT}(\mathbf{R})$ from WM iron, WM myelin, GM iron, while the ventricles have zero susceptibility. (B) shows the corresponding frequency shift $\overline{\Omega}_{MRI}(\mathbf{R})$ from $\delta\overline{\chi}_{GT}(\mathbf{R})$ including frequency shifts from a uniform external and internal susceptibility. (C) shows $\overline{\Omega}_{MRI}(\mathbf{R})$ after background field removal, which removes both contributions from the internal and external uniform susceptibility. (D) Shows the difference between the fitted susceptibility $\delta\overline{\chi}_{Fit}(\mathbf{R})$ (after referencing to CSF in ventricles) and ground truth susceptibility $\delta\overline{\chi}_{GT}(\mathbf{R})$.

FIGURE S2. Overview of pipeline for MGE processing: All the complex MGE images were MP-PCA denoised, and Gibbs-unrung. The complex phase was extracted, unwrapped and background-field corrected, and subsequently fitted to extract $\overline{\Omega}_{MRI}$. $\overline{\Omega}_{Background}$ shows the subtracted background frequency. Representative signal magnitude (left plot) and unwrapped and background-field corrected phase (right plot) are plotted for a white matter (cingulum in blue) and gray matter (thalamus in orange) voxel, respectively. Magnitude is shown in semi-log scale to illustrate the mono-exponential behavior of both signals are predominantly mono exponential. The phase behaves linearly in both WM and GM.

FIGURE S3. Overview of dMRI pipeline for data processing: The Complex dMRI images were tensor MP-PCA denoised for each echo time individually followed by Gibbs-unringing. The signal magnitudes were then averaged over echo times using SVD, and the resulting images were then fitted with DKI or FBI for tensor or fODF estimation. Color-coded FA maps from diffusion tensor ($FA_{\mathbf{D}}$) and scatter matrices ($FA_{\mathbf{T}}$, cf. Equation (12) in Supplementary Information S2) from FBI are shown for various protocols. $S(b,\hat{\mathbf{g}})$ denotes the dMRI signal with b-value along $\hat{\mathbf{g}}$, here the in-plane direction $\hat{\boldsymbol{z}}$ (green on sphere).

FIGURE S4. Populations of cylinders with different levels of orientation dispersion are shown in (A). (B) shows the probability density function (pdf) of the resulting cylinder parameters for each configuration. The cylinder radius ρ is gamma-distributed, while θ and φ are uniformly distribution in the full range of azimuthal angle and from zero to the maximum polar angle θ_c, respectively. Colors are used to represent different populations with orientation dispersion indicated by the colorbar.

FIGURE S5. Optimal number of iterations and Tikhonov in phantom simulation: The optimal number of iterations and Tikhonov regularization are shown for each algorithm and for each configuration of magnetic susceptibility. QSM+ requires more iterations to converge to the optimal solution but requires less regularization than QSM.

FIGURE S6. Susceptibility maps of mouse brain at 100 μm isotropic resolution: Horizontal slices from the medial and anterior parts of the brain are shown. $\overline{\chi}_{QSM}$ corresponds to zero mesoscopic contribution (analogous to QSM), and $\overline{\chi}_{QSM+}$ corresponds to a non-zero mesoscopic contribution calculated using this method.

FIGURE S7. Susceptibility maps of mouse brain at 100 μm isotropic resolution: Sagittal slices from the medial and anterior parts of the brain are shown. $\overline{\chi}_{QSM}$ corresponds to zero mesoscopic contribution (analogous to QSM), and $\overline{\chi}_{QSM+}$ corresponds to a non-zero mesoscopic contribution calculated using this method.

FIGURE S8. COSMOS Susceptibility fitting of rat brain at 150 μm isotropic resolution: The plot to the left show voxel-by-voxel comparison of the residuals $\delta\overline{\Omega}_{MRI}$ for fitting including all orientations. The red line corresponds to the unit line, while the blue shows a linear fit, with slope below 1, indicating lower residuals with QSM+. $\sigma^2_{\hat{\mathbf{B}}}\left(\delta\overline{\Omega}_{MRI}\right)$ shows the variance in the residuals for a coronal slice of the rat brain in the anterior part of the brain.

FIGURE S9. COSMOS Susceptibility maps of rat brain at 150 μm isotropic resolution: Coronal slices from the anterior part of the brain are shown. $\overline{\chi}_{QSM}$ corresponds to zero mesoscopic contribution (conventional COSMOS), and $\overline{\chi}_{QSM+}$ includes a non-zero mesoscopic contribution calculated using this method.

FIGURE S10. Susceptibility fitting of rat brain at 150 μm isotropic resolution at five different orientations: The plots to the left show voxel-by-voxel comparison of the residuals $\delta\overline{\Omega}_{MRI}$ for each sample orientation labeled in the title. Nan corresponds to no rotation (two individual experiments are shown), and here the field is along the sagittal orientation of the brain. The red line corresponds to the unit line, while the blue shows a linear fit, with slope slightly below 1, indicating lower residuals with QSM+. $\sigma^2_{\hat{\mathbf{B}}}\left(\delta\overline{\Omega}_{MRI}\right)$ and $\sigma^2_{\hat{\mathbf{B}}}(\delta\overline{\chi})$ show the variance in the residuals and susceptibility fits, respectively, for a coronal slice of the rat brain in the anterior part of the brain.

How to cite this article: Sandgaard AD, Kiselev VG, Henriques RN, Shemesh N, Jespersen SN. Incorporating the effect of white matter microstructure in the estimation of magnetic susceptibility in ex vivo mouse brain. *Magn Reson Med*. 2024;91:699-715. doi: 10.1002/mrm.29867